Chemical Engineering Journal 430 (2022) 133061

Contents lists available at ScienceDirect

Chemical Engineering Journal

journal homepage: www.elsevier.com/locate/cej

Facile morphology control strategy to enhance charge separation efficiency of Mo:$BiVO_4$ photoanodes for efficient photoelectrochemical water splitting

Sang Gi Shim [1], Jeiwan Tan [1], Hyungsoo Lee, Jaemin Park, Juwon Yun, Young Sun Park, Kyungmin Kim, Jeongyoub Lee, Jooho Moon [*]

Department of Materials Science and Engineering, Yonsei University, 50 Yonsei-ro, Seodaemun-gu, Seoul 03722, Republic of Korea

ARTICLE INFO

Keywords:
Photoelectrochemical water splitting
Bismuth vanadate
Photoanode
Nanostructuring
Pore former

ABSTRACT

Bismuth vanadate ($BiVO_4$) is one of the promising earth-abundant semiconducting materials for photoelectrochemical (PEC) water splitting. However, $BiVO_4$ suffers from poor charge separation efficiency due to its low carrier mobility and short minority carrier diffusion length. Nanostructured $BiVO_4$ photoanodes provide a simple way to improve charge separation efficiency. Here, we propose a facile nanostructuring strategy for enhancing the PEC performance of molybdenum-doped $BiVO_4$ (Mo:$BiVO_4$) photoanodes by varying the molecular weight of poly(ethylene glycol) (PEG) as a pore former. It was demonstrated that the grain and pore sizes of Mo:$BiVO_4$ could be controlled by changing the molecular weight of PEG. Nanoporous Mo:$BiVO_4$ photoanodes with optimized grain and pore sizes revealed an effective charge separation efficiency of 72% and showed the highest photocurrent density of 2.2 mA cm^{-2} at 1.23 V versus the reversible hydrogen electrode (V_{RHE}). After hydrogen treatment and decoration of nickel iron (oxy)hydroxide (NiFeOOH) as an oxygen evolution catalyst, a stable photocurrent density of 4.5 mA cm^{-2} with a 10-h duration was achieved at 1.23 V_{RHE} under standard 1-sun illumination. Our findings clearly suggest new insights on a simple strategy to improve the PEC performance of nanostructured Mo:$BiVO_4$ photoanodes.

1. Introduction

Photoelectrochemical (PEC) water splitting, which generates hydrogen using sunlight, has been suggested as an eco-friendly and renewable fuel production strategy to replace fossil fuels [1]. In a typical PEC cell, a semiconductor produces electron–hole pairs by absorbing photons of energy equal to or higher than its band gap that carry out the water reduction–oxidation process on the surface of the photoelectrode. Because the water oxidation involving a four-hole transfer process is considered to be the rate-determining step in PEC water splitting, many PEC research studies have aimed to develop highly efficient photoanodes. Generally, metal oxides are considered attractive photoanode materials due to their low-cost synthesis and higher stability than other semiconductors [2]. Among them, bismuth vanadate ($BiVO_4$) exhibits great promise owing to its high photocurrent density around 4–6 mA cm^{-2}, which is close to its theoretical photocurrent density of 7.5 mA cm^{-2} (based on the band gap of 2.4 eV); high photovoltage of ~ 1 V; and photochemical stability in near-neutral aqueous medium [3]. However, the PEC performance of $BiVO_4$ photoelectrodes is limited due to their poor charge separation efficiency caused by their low carrier mobility (<1 cm^2 V^{-1} s^{-1}) and short hole diffusion length [4]. In this regard, a viable strategy to enhance the charge separation efficiency is required to achieve high-performance $BiVO_4$ photoelectrodes.

Previous reports have suggested that either the substitutional doping of V^{5+} with metal ions such as $Mo^{6+}$and W^{6+} or the creation of oxygen vacancies via H_2 or N_2 posttreatment could enhance the charge separation efficiency because of the improved electrical conductivity of doped $BiVO_4$ [5]. Other studies have suggested that the built-in electric field induced by band bending through the formation of heterojunctions (e.g., $BiVO_4$/WO_3) [6,7] or coating of oxygen evolution reaction (OER) catalysts (e.g., nickel iron oxide ($NiFeO_x$) [8], Co-Pi [9], and MnO_x [10]) could promote charge separation. However, the heterogeneous interface formation and aliovalent doping might cause charge recombination due to the increased trap sites. The simplest way to improve the charge separation efficiency is to nanostructure $BiVO_4$ photoanodes, shortening the carrier travel distance so that more photogenerated holes can

* Corresponding author.
E-mail address: jmoon@yonsei.ac.kr (J. Moon).
[1] These authors contributed equally.

https://doi.org/10.1016/j.cej.2021.133061
Received 17 July 2021; Received in revised form 12 October 2021; Accepted 13 October 2021
Available online 20 October 2021

participate in the OER without the detrimental recombination. Various researchers have engineered the dimensional morphology, porosity and crystallographic orientation of film, while these nanostructured photoanodes have additional advantages of desirable optoelectronic properties including large specific surface area and efficient light absorption [11–16]. However, how the grain size of $BiVO_4$ affects the charge separation efficiency is hardly investigated. Indeed, the grain size of a photoelectrode can play an important role in achieving high PEC performance, as the charge transport and surface band bending may vary depending on the grain size. [11,17–19].

A variety of nanostructured $BiVO_4$ photoanodes such as nanorods and nanoporous structures have been fabricated by the hydrothermal technique, microwave-assisted synthesis, and electrodeposition [20–22]. However, the hydrothermal method is generally time-consuming and microwave-assisted synthesis requires complex equipment, while electrodeposition inevitably involves secondary phase formation, deteriorating the phase purity of $BiVO_4$ [22,23]. Therefore, there is a need for a strategy enabling the nanostructuring of $BiVO_4$ photoanodes without complicated processes and equipment. One possible method, metal organic decomposition (MOD), involves using a precursor solution of Bi and V in the presence of poly(ethylene glycol) (PEG) [24–27]. PEG is considered a suitable morphology-directing agent due to its non-toxicity, high solubility in many organic solvents, and easy decomposability without residue. The role of PEG as a pore former or pore size controller has been investigated by varying the amount of PEG. For example, Feng et al. demonstrated pore size–controlled nanoporous $BiVO_4$ photoanodes by adjusting the amount of commercial PEG product (i.e., PEG 600, whose average molecular mass is 570–630). The optimized nanoporous $BiVO_4$ photoanodes showed 3.5 mA cm^{-2} at 0.7 V_{RHE} during sulfite oxidation. The enhanced PEC performance of nanoporous $BiVO_4$ originated from the enhanced charge separation efficiency due to the enlarged surface area and multiple light scattering induced by nanostructuring [26]. Furthermore, PEG is capable of not only increasing the surface area but also controlling the grain size of the photoelectrode [28,29]. Meda et al. demonstrated grain size–controlled WO_3 photoanodes by varying the molecular weight of various dispersants, including PEG, while they were unable to fully elucidate its role in altering grain size [30].

Herein, we propose a facile nanostructuring strategy of molybdenum-doped $BiVO_4$ (Mo:$BiVO_4$) photoanodes with the aid of PEG. Particle-like morphology with controlled grain and pore sizes for Mo:$BiVO_4$ was obtained by varying the molecular weights of PEG in the precursor solution. Microstructural analysis revealed that the PEG can affect the grain growth rate, thereby determining the grain size and pore structure. In addition, the bulk charge separation efficiency of nanostructured Mo:$BiVO_4$ was changed depending upon the grain size, in turn affecting the PEC performance. The nanostructured Mo:$BiVO_4$ with large grain size not only induced large surface band bending but also retained low bulk transport resistance so that the charge carriers were easily separated and injected into the electrolyte without bulk recombination. Owing to the improved optoelectronic properties of nanostructured Mo:$BiVO_4$, the bulk charge separation efficiency increased up to 89% at 1.23 V_{RHE} after the modification with hydrogen treatment. Finally, the optimized Mo:$BiVO_4$ photoanodes demonstrated the photocurrent density of 4.5 mA cm^{-2} at 1.23 V_{RHE} as well as stable operation for 10 h after decoration with a NiFeOOH co-catalyst.

2. Experimental Section

2.1. Fabrication of tin oxide (SnO_2) film

The FTO glass substrates (TEC-8, Pilkington, UK) were ultrasonically cleaned in acetone (Duksan Pure Chemicals, Korea), deionized (DI) water, and isopropyl alcohol (IPA, Duksan Pure Chemicals, Korea) for 15 min, respectively, followed by UV treatment for 15 min. After cleaning, the SnO_2 film was prepared using the sol–gel process [30]. Briefly, 50 mmol of $SnCl_2{\cdot}2H_2O$ (Sigma-Aldrich, 98%, USA) was dissolved in 5 ml of IPA. The precursor solution was spin coated on the FTO substrate at 2000 rpm for 30 s followed by annealing at 500 °C for 1 h on a hot plate under ambient conditions.

2.2. Fabrication of Mo:$BiVO_4$ PEG photoanodes

First, 0.5 mol of $Bi(NO_3)_3{\cdot}5H_2O$ (Sigma-Aldrich, 98%) was dissolved in 5 ml of glacial acetic acid (Duksan Pure Chemicals, Korea), and 0.075 mol of $VO(acac)_2$ (Sigma-Aldrich, 98%) solution was prepared with 5 ml of methanol (Duksan Pure Chemicals, Korea). For the Mo solution, 0.075 mol of $MoO_2(acac)_2$ (Sigma-Aldrich, 98%) was dissolved in 5 ml of methanol. Each precursor was mixed with the stoichiometric molar ratio of Bi:(V + Mo) = 1:1 where the Mo doping concentration was 1 at% for Mo:$BiVO_4$ photoanodes. For Mo:$BiVO_4$ PEG precursor solutions, PEG 200 (molecular mass 190–210), PEG 300 (molecular mass 285–310), or PEG 400 (molecular mass 380–420) (Sigma-Aldrich) was added to Mo:$BiVO_4$ precursor solutions after 20 min of ultrasonification. The amount of PEG added was fixed as the volume ratio between vanadium (V) precursor solution : PEG = 1 : 0.2 regardless of PEG molecular weight. The Mo:$BiVO_4$ PEG solutions were then spin coated on the FTO/SnO_2 substrate at 1500 rpm for 20 s. After the spin coating, the substrates were immediately annealed on a hot plate at 400 °C for 7 min under ambient air conditions. The repeated spin-coating and annealing processes were performed seven times to obtain a desired and followed by annealing at 480 °C for 30 min in a box furnace with a ramping rate of 10 °C per min. Finally, copper wire and silver paste were employed to form a contact with the electrode. Epoxy resin (Hysol 9642, Henkel, Düsseldorf, Germany) was selectively applied for covering the electrode excluding an active area (~0.1 cm^2) exposed to the electrolyte.

2.3. Hydrogen treatment of Mo:$BiVO_4$ PEG film

For hydrogen treatment, the Mo:$BiVO_4$ films were annealed under a 5% H_2/95% Ar atmosphere in a tube furnace. The flow rate was kept constant at 200 sccm, and the heating rate was 10 °C per min. Annealing temperatures of 200–300 °C were used with a fixed duration of 20 min.

2.4. NiFeOOH deposition on surface of Mo:$BiVO_4$ PEG film

The NiFeOOH co-catalysts were deposited by photo-assisted electrodeposition (PED) under AM 1.5 G illumination according to the reported procedure [8]. Briefly, 60 mg of $FeSO_4{\cdot}7\ H_2O$ (≥99%; Sigma-Aldrich) and 20 mg of $NiSO_4{\cdot}6H_2O$ (99%; Sigma-Aldrich) were dissolved in 200 ml of 0.5 M potassium hydrogen carbonate ($KHCO_3$) aqueous solution. The solution was purged with Ar gas before and during the deposition. For deposition, under standard 1-sun illumination, linear sweep voltammetry (LSV) was conducted with a bias from − 0.3 V to 0.5 V against the reference electrode (Ag/AgCl/KCl (4 M)) 18–22 times with pretreatment of − 0.3 V for 5 s. The scan rate was 50 mV s^{-1}. After deposition, the photoelectrode was washed with copious amounts of DI water and dried at 100 °C for 1 h under ambient air conditions on a hot plate.

2.5. Characterization of optical and structural properties

The surface and cross-sectional microstructures of the Mo:$BiVO_4$ photoanodes were examined using a field emission scanning electron microscope (SEM, JSM-IT500HR, JEOL, Japan). The mean grain size and pore size of the Mo:$BiVO_4$ photoanodes were obtained by measuring the diameters of 100 randomly selected grains as shown in the SEM images. To estimate the porosity and pore size, the SEM images were analyzed using ImageJ software (Wayne Rasband, National Institutes of Health, USA). A UV–vis spectrophotometer equipped with an integrating sphere (V-670, JASCO, Easton, MD, USA) was employed for determining the optical properties of the Mo:$BiVO_4$ photoanodes. The

crystal phase was determined using X-ray diffraction (XRD) (MiniFlex 600, Rigaku, Japan) with Cu K_α radiation ($\lambda = 0.15406$ nm). The θ-2θ scan mode was used for the XRD analysis. The surface chemical information of Mo:$BiVO_4$ before and after the H_2 treatment was analyzed via X-ray photoelectron spectroscopy (XPS, K-alpha, Thermo Scientific Inc., UK). All XPS spectra were calibrated using the C 1 s peak, which has a binding energy of 284.6 eV, and the background was fitted using the Shirley method; fitting curves for the deconvolution of O 1 s peak were determined using a Gaussian peak function. Transmission electron microscopy (TEM) and elemental mapping were performed using a JEM-200F (JEOL, Japan) equipped with an energy-dispersive X-ray spectrometer (EDS) at an acceleration voltage of 200 kV.

2.6. PEC characterizations

The PEC measurements, including LSV and chronoamperometry, were conducted using a potentiostat (SI 1287, Solartron, UK) with a typical three-electrode system with an Ag/AgCl/KCl (4 M) reference electrode and a Pt wire as the counter electrode. A commercial AM 1.5 G solar simulator and a Si reference cell (Newport Corporation, USA) were utilized for the simulated sunlight and 1-sun calibration, respectively. The applied potentials were based on the reversible hydrogen electrode (RHE) scale for comparison with other reports. The following equation was used to convert the potential:

$$E_{RHE} = E_{Ag/AgCl} + 0.0591\,pH + 0.197 \quad (1)$$

EIS was conducted using the same potentiostat, along with a frequency analyzer (1260, Solartron, Leicester, UK). The series (R_s) and polarization resistance (R_p) of the Mo:$BiVO_4$ photoanodes were measured in 0.5 M potassium phosphate buffer (KPi) containing 0.5 M Na_2SO_3 (pH = 7.1) with the frequency range of 100 kHz to 1 Hz under 1-sun illumination at 0.8 V_{RHE} with an alternating-current amplitude of 10 mV. The M−S analysis was measured in 0.5 M KPi (pH = 7) under dark conditions with an amplitude of 10 mV at a frequency of 1 kHz. The incident photon to conversion efficiency (IPCE) measurements were conducted using an electrochemical workstation (Zennium, Zahner, Germany) and a potentiostat (PP211, Zahner, Germany) with a monochromatic light source (TLS03, Zahner) under 0.5 M KPi (pH = 7) at 1.23 V_{RHE} with the same three-electrode configuration.

2.7. Estimation of donor density and flat band potential

The M−S analysis was conducted in 0.5 M KPi (pH = 7) under dark conditions with a frequency of 1 kHz and an amplitude of 10 mV to obtain the donor density (N_d) and flat band potential (E_{fb}). The capacitance of the space charge layer (C_{sc}) can be expressed by the following equation:

$$C_{sc}^{-2} = \frac{2}{\varepsilon_o \varepsilon_r e A^2 N_d}\left(E - E_{fb} - \frac{K_B T}{e}\right) \quad (2)$$

where ε_o is the vacuum permittivity (8.854×10^{-12} F m^{-1}), ε_r is the relative permittivity of $BiVO_4 \sim 86$ [26], e is the electron charge (1.602×10^{-19}C), A is the surface area of the photoelectrode, E is the applied potential, E_{fb} is the flat band potential, k_B is the Boltzmann constant (1.381×10^{-23} J K^{-1}), and T is the absolute temperature. The x-axis intercept of the tangent line in the plot indicates the flat band potential of the electrode.

Then, N_d can be calculated as follows:

$$N_d = \frac{2}{\varepsilon_0 \varepsilon_r e}\left(\frac{d\left(C_{sc}^{-2}\right)}{dE}\right)^{-1} \quad (3)$$

2.8. Estimation of bulk charge separation efficiency and charge injection efficiency:

The measured photocurrent density from the water oxidation reaction (J^{OER}) can be expressed as follows:

$$J^{OER} = J_{max} \times \eta_{abs} \times \eta_{bulk} \times \eta_{inj} = J_{abs} \times \eta_{bulk} \times \eta_{inj} \quad (4)$$

where J_{max} is the maximum theoretical photocurrent density, η_{abs} is the light absorption efficiency, and J_{abs} is the maximum photocurrent density based on light absorption, whereas η_{bulk} and η_{inj} indicate the bulk charge separation efficiency and charge injection efficiency, respectively. J_{abs} can be calculated as follows:

$$J_{abs} = \int_{\lambda_1}^{\lambda_2} \frac{\lambda}{1240} P_{abs}(\lambda) d\lambda \quad (5)$$

where λ_1 and λ_2 are 300 nm and 515 nm, respectively, when considering the absorption edge of the $BiVO_4$ band gap energy (2.4 eV). P_{abs} indicates the actual power of light absorbed by the Mo:$BiVO_4$ photoanodes, which can be presented as follows:

$$P_{abs}(\lambda) = P_o \times LHE \quad (6)$$

where P_o is the power of light provided by the solar simulator (AM 1.5 G, 100 mW cm^{-2}) and LHE represents light harvesting efficiency which can be written as follows:

$$LHE = 1\text{-}10^{-A_{(\lambda)}} \quad (7)$$

($A_{(\lambda)}$: absorbance at wavelength λ)

Since the charge injection efficiency can be assumed to be almost 100% (i.e., $\eta_{inj} = 1$) when a sacrificial agent (i.e., sulfite ion (SO_3^{2-})) is involved, the photocurrent density obtained from the SO_3^{2-} oxidation reaction (J^{SOR}) can be expressed as follows:

$$J^{SOR} = J_{abs} \times \eta_{bulk} \quad (8)$$

Then, η_{bulk} can be expressed as follows:

$$\eta_{bulk} = J^{SOR}/J_{abs} \quad (9)$$

and η_{inj} can be expressed as follows:

$$\eta_{inj} = J^{OER}/J^{SOR} \quad (10)$$

2.9. Estimation of applied bias photon-to-current efficiency (ABPE) of Mo:$BiVO_4$ photoanodes and O_2 evolution

The ABPE efficiency of the Mo:$BiVO_4$ photoanodes can be calculated using the following equation:

$$ABPE(\%) = \left(\frac{J^{OER} \times (1.23 - V)}{P_o}\right) \quad (11)$$

where J^{OER} is the photocurrent density (mA cm^{-2}) of water oxidation, V is the applied bias (volts), and P_o is the power density provided by the solar simulator (AM 1.5 G, 100 mW cm^{-2}).

GC (6500GC system, YL Instrument, Anyang, Korea) was performed using a pulsed discharge detector and a molecular sieve column to analyze the O_2 evolution. All the connections of the device were completely sealed with rubber bulkheads to prevent gas leakage from the quartz tubes. The Faradaic efficiency was defined as the ratio of the rate of oxygen evolution to that of $e^-/4$. The active area of the photoelectrode for this measurement was 0.3 cm^2.

3. Results and discussion

3.1. Morphology of Mo:$BiVO_4$ films depending upon the molecular weight of PEG

Mo:$BiVO_4$ films were fabricated onto a fluorine-doped tin oxide (FTO)/SnO_2 substrate by spin coating using a Mo:$BiVO_4$ homogeneous precursor solution with 1 at% Mo concentration composed of

stoichiometric metal ions and PEG. The as-spin-coated films were immediately placed on a hot plate followed by annealing at 400 °C in air for 7 min (Fig. 1, see Experimental Section for details). Compared to conventional nanostructuring method for $BiVO_4$, our fabrication did not involve a complex process, expensive equipment, or time-consuming treatment to obtain nanostructured Mo:$BiVO_4$ photoanodes. The reference electrode without any addition of PEG in the precursor solution (denoted as Mo:$BiVO_4$ w/o PEG) exhibited a pinhole-free dense microstructure with a film thickness of 225.4 ± 11 nm (Fig. 2**a**). By adding PEG to the precursor solution, we observed particulate films with different sizes of grains and pores depending on the molecular weight of PEG (Fig. 2**b–d**). Each PEG-added film was denoted as Mo:$BiVO_4$ PEG × where × refers to the molecular weight of PEG which can be calculated as 44.05n + 18.02 g/mol, where n is the number of repeating monomer (i.e., ethylene glycol (EG)). The average n value of PEG 200, PEG 300, and PEG 400 is 4, 6, and 8, respectively. The Mo:$BiVO_4$ PEG 200 photoanodes exhibited an average grain size of 278.4 ± 44 nm with a film thickness of 234.4 ± 12 nm as determined by image analysis. With the increasing molecular weight of PEG, the Mo:$BiVO_4$ PEG photoanodes showed a decreasing grain size while maintaining a similar film thickness. Mo:$BiVO_4$ PEG 300 showed a grain size of 220.3 ± 31 nm, which was further reduced to 155.7 ± 27 nm for Mo:$BiVO_4$ PEG 400, whereas the film thickness remained in the range of 232.8 ± 6 nm and 225.9 ± 8 nm (see **Table S1**, Supplementary Information). Moreover, Mo:$BiVO_4$ PEG 200 exhibited the largest pore size of 199.1 ± 32 nm followed by Mo:$BiVO_4$ PEG 300 (164.1 ± 50 nm) and Mo:$BiVO_4$ PEG 400 (83.7 ± 32 nm). In the case of Mo:$BiVO_4$ PEG 400, a higher porosity of 53.0% was observed compared to that of Mo:$BiVO_4$ PEG 300 (38.9%) and Mo:$BiVO_4$ PEG 200 (27.7%). This is presumably due to the increased number of small pores resulting from decreasing the grain size of Mo:$BiVO_4$ PEG 400 (see **Table S2**, Supplementary Information).

To investigate the effect of PEG molecular weight on the morphology of Mo:$BiVO_4$, thermogravimetric (TG) and differential scanning calorimetry (DSC) analyses were conducted with Mo:$BiVO_4$ PEG precursor solutions. As shown in Fig. 3a, all precursor solutions similarly showed a broad endothermic peak near 250 °C due to the vaporization of residual solvents and decomposition of organic ligands. It is considered that the first exothermic peak accompanying the major weight loss observed at ~ 300 °C corresponds to the crystallization of Mo:$BiVO_4$ upon the combustion of PEG [31]. The second exothermic peak observed at 400–450 °C represented the phase transition from a tetragonal to monoclinic-scheelite crystal structure. Notably, this exothermic peak involving the crystallization was shifted to a higher temperature with the increasing molecular weight of PEG. The peak was observed at 312 °C for Mo:$BiVO_4$ PEG 200, whereas it shifted to 326 °C for Mo:$BiVO_4$ PEG 300 and 334 °C for Mo:$BiVO_4$ PEG 400 (Fig. 3b). This peak shift indicated that high-molecular-weight PEG could delay the crystallization of Mo:$BiVO_4$. Considering the fabrication procedure, after the initial spin coating and annealing at 400 °C for 7 min, a thin Mo:$BiVO_4$ layer (~30 nm) should be formed after complete pyrolysis of PEG and solvent evaporation (dry film). As-formed Mo:$BiVO_4$ grains individually play a role as a small nuclei for the following step of spin coating in which the metal-PEG complex solution covers the Mo:$BiVO_4$ layer (wet film). It was demonstrated that the metal-PEG complex is formed by strong interaction between ether oxygens of PEG and dissolved metal ions [32,33]. During the next annealing and crystallization process, the as-formed Mo:$BiVO_4$ nuclei grow by the classical nuclei growth mechanism which is the ion-by-ion addition through diffusion to the formed crystal [13,34]. However, the Mo:$BiVO_4$ could be interfered by surrounding PEG chains which are strongly bonded to metal ions, suppressing the crystal growth [35–37]. Moreover, the longer chain length (i.e., higher molecular weight) of PEG can severely hinder the nuclei growth from the metal ion addition during the crystallization process [38]. Therefore, it is reasonable to assume that the presence of higher-molecular-weight PEG within the wet film reduces the growth rate of nuclei, resulting in small-grain-sized Mo:$BiVO_4$ film.

The influence of an additive with a shorter chain length than PEG 200 on the morphology of Mo:$BiVO_4$ photoanodes was also investigated by adding to the precursor solution EG and diethylene glycol (DEG), both of which have a shorter chain length (i.e., lower molecular weight) than PEG 200 (**Fig. S1a,b**, Supplementary Information). The Mo:$BiVO_4$ EG film revealed a large grain size of 406 ± 96 nm with a thickness of 239.8 ± 6 nm, whereas Mo:$BiVO_4$ DEG exhibited a small grain size of 118.1 ± 30 nm with a thickness of 224.5 ± 6 nm and occasional pinholes. While the grain sizes differed significantly, both samples exhibited a dense film-like morphology rather than the nanoporous structure associated with Mo:$BiVO_4$ PEG films. It is considered that additives having relatively short chains do not significantly affect the metal ion

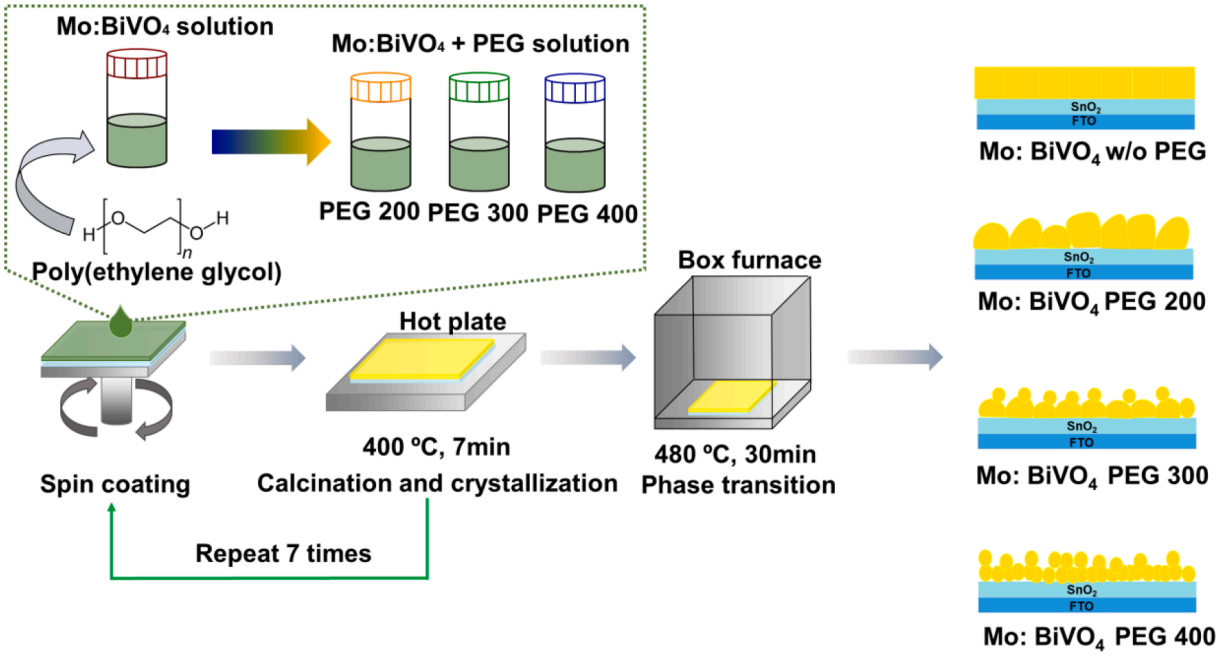

Fig. 1. Schematic showing synthesis sequences for Mo:$BiVO_4$ photoanodes fabricated by facile spin-coating method.

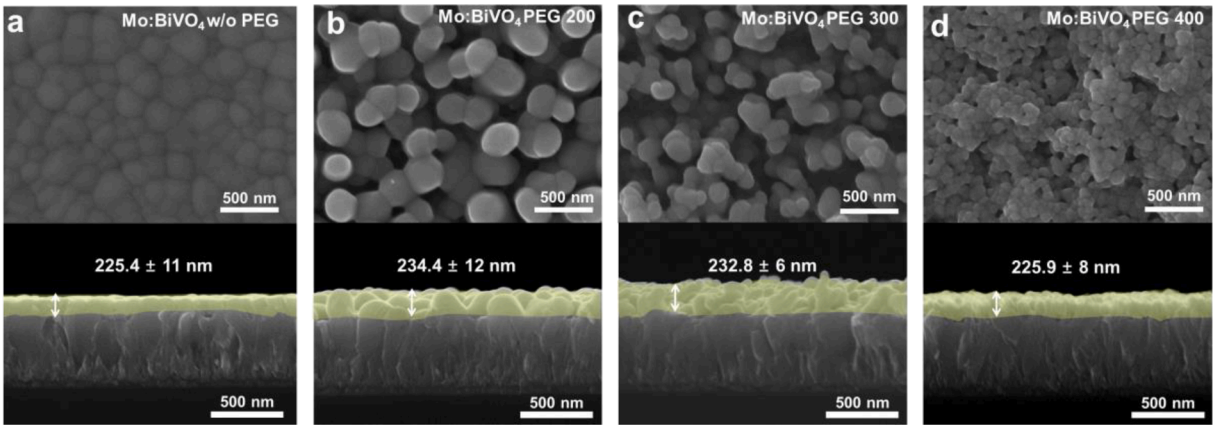

Fig 2. Top-view and cross-sectional SEM images of a) Mo:$BiVO_4$ w/o PEG, b) Mo:$BiVO_4$ PEG 200, c) Mo:$BiVO_4$ PEG 300, and d) Mo:$BiVO_4$ PEG 400. The volume ratio between vanadium (V) precursor solution and PEG (i.e., V : PEG) was kept to 1 : 0.2 for each Mo:$BiVO_4$ PEG film.

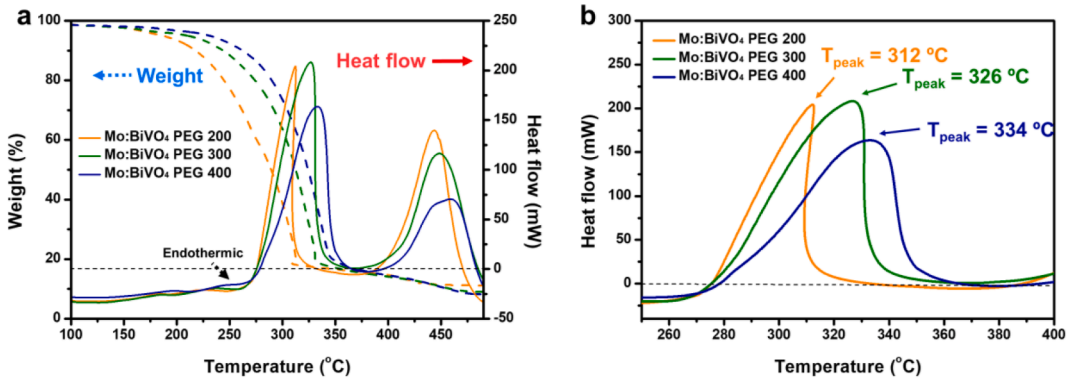

Fig. 3. a) TG analysis and DSC plots obtained from Mo:$BiVO_4$ precursor solution with PEG additive: PEG 200 (orange), PEG 300 (green), and PEG 400 (navy). b) Magnified DSC plot near crystallization temperature of Mo:$BiVO_4$. The ramp rate was 10 °C min^{-1}. (For interpretation of the references to colour in this figure legend, the reader is referred to the web version of this article.)

addition during the growth and that the pores resulting from the elimination of additives can be easily filled by grain growth, leading to a compact film morphology. On the other hand, the additives with longer chains (i.e., PEG 200 to PEG 400) readily hinder the nuclei growth by ion addition and surface reaction during the crystallization process, reducing the grain size and resulting in a nanoporous structure (**Fig. S2**, Supplementary Information). The crystallinity and phase of Mo:$BiVO_4$ photoanodes as a function of PEG molecular weight were revealed by XRD (**Fig. S3a,b**, Supplementary Information). All Mo:$BiVO_4$ photoanodes showed peak splitting at $2\theta \sim 34.8°$ and 35.4° corresponding to the (200) and (020) planes, respectively. The observed peak splitting at $2\theta \sim 35°$ indicates that Mo:$BiVO_4$ photoanodes have a monoclinic scheelite crystal structure (JCPDS No. 00–014-0688) without any secondary phase or impurities regardless of PEG molecular weight, implying that the Mo was successfully doped into the $BiVO_4$ lattice [39]. Moreover, the relative peak intensity of the (200) and (020) planes became broader with the increasing PEG molecular weight, indicative of the decreased crystal size for the Mo:$BiVO_4$ films, which is consistent with the tendency observed in Fig. 2.

3.2. Optical and PEC properties of Mo:$BiVO_4$ photoanodes

The influence of different morphologies on the light absorption properties of Mo:$BiVO_4$ photoanodes was investigated by ultraviolet–visible (UV–vis) spectroscopy (Fig. 4a). All photoanodes with PEG clearly showed enhanced light absorption with respect to the sample without PEG. Note that the light absorption spectra were obtained by subtracting the transmittance and reflectance from unity (**Fig. S4**, Supplementary Information), Considering the band gap of $BiVO_4$ (2.4 eV), the absorbance over 515 nm which is the light absorption edge, does not represent the actual absorption by $BiVO_4$. Assuming 100% absorbed photon-to-current conversion efficiency (APCE), the maximum achievable photocurrent from Mo:$BiVO_4$ photoanodes was calculated by integrating the LHE and photon flux of the light in the range from 300 nm to 515 nm. The calculated maximum achievable photocurrent densities were 5.19, 5.08, and 4.83 mA cm^{-2} for Mo:$BiVO_4$ PEG 200, Mo:$BiVO_4$ PEG 300, and Mo:$BiVO_4$ PEG 400, respectively, higher than that of Mo:$BiVO_4$ w/o PEG (4.15 mA cm^{-2}) (**Table S3**, Supplementary Information). Furthermore, we determined the η_{abs} for Mo:$BiVO_4$ films by dividing the maximum achievable photocurrent density by J_{max} of 7.5 mA cm^{-2} obtained from $BiVO_4$'s band gap of ~ 2.4 eV. The resulting η_{abs} was determined to be 69.2% for Mo:$BiVO_4$ PEG 200, 67.7% for Mo:$BiVO_4$ PEG 300, 64.4% for Mo:$BiVO_4$ PEG 400, and 55.3% for Mo:$BiVO_4$ w/o PEG. Because the thickness for all Mo:$BiVO_4$ photoanodes was nearly identical, the enhanced η_{abs} in Mo:$BiVO_4$ PEG photoanodes could be attributed to enhanced light absorption by the multiple light scattering occurring in the particulate arrays and pores within the Mo:$BiVO_4$ PEG films. It has been reported that incident light can be trapped in the pores involved in Mo:$BiVO_4$ PEG photoanodes, leading to multiple internal scattering [26,40]. Therefore, more light can be absorbed in Mo:$BiVO_4$ PEG photoanodes due to the reduced reflection in the range from 300 nm to 515 nm (**Fig. S4**, Supplementary Information).

To gain insight on the influence of different Mo:$BiVO_4$ morphologies on PEC performance, we performed LSV. Fig. 4b shows the photocurrent for water oxidation (J^{OER}) versus applied potential measured in 0.5 M

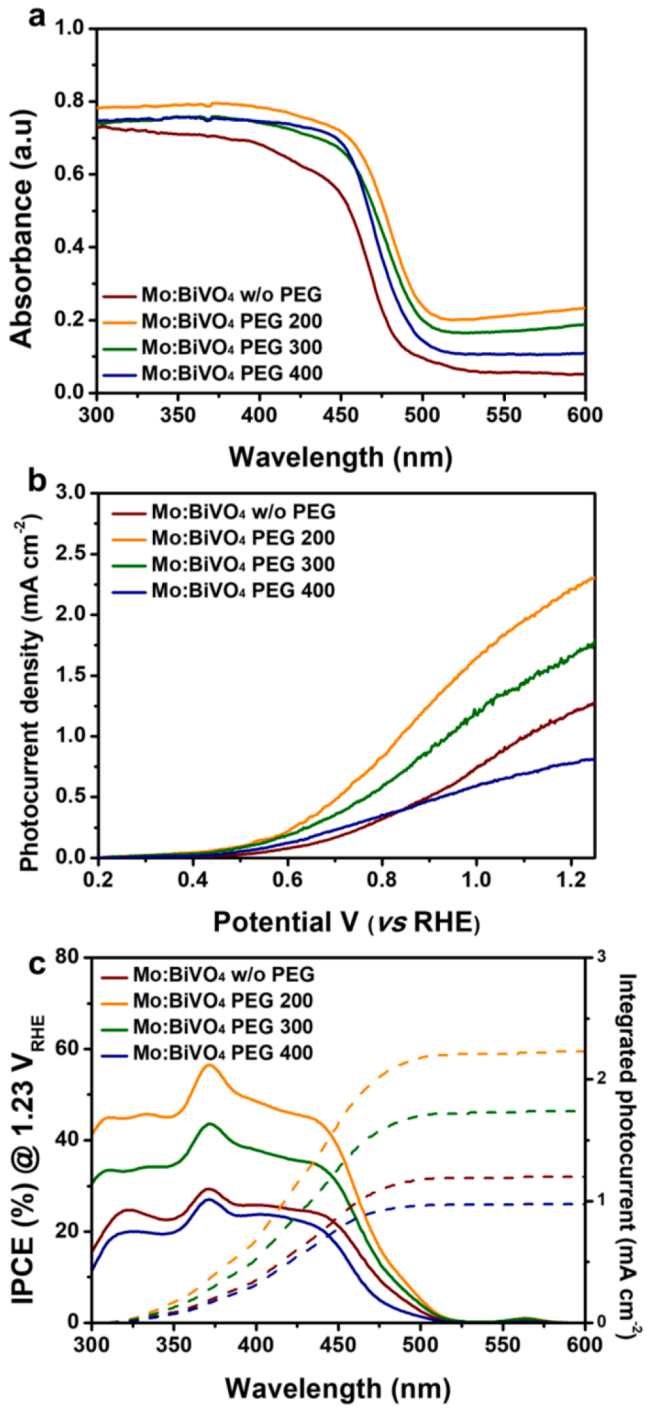

Fig. 4. a) Light absorption properties of Mo:$BiVO_4$ photoanodes investigated by UV–vis analysis. b) Photocurrent density for water oxidation (J^{OER}) versus applied potential for Mo:$BiVO_4$ w/o PEG (maroon), Mo:$BiVO_4$ PEG 200 (orange), Mo:$BiVO_4$ PEG 300 (green), and Mo:$BiVO_4$ PEG 400 (navy) measured in 0.5 M KPi (pH = 7) under front-side 1-sun illumination at scan rate of 20 mV s^{-1}. c) IPCE spectra of Mo:$BiVO_4$ photoanodes measured in 0.5 M KPi (pH = 7) at 1.23 V_{RHE}. (For interpretation of the references to colour in this figure legend, the reader is referred to the web version of this article.)

KPi (pH = 7) under standard front-side illumination (1-sun AM 1.5 G). The onset potential defined as the potential at which the photocurrent curve begins was observed to be 0.5–0.6 V_{RHE} for all Mo:$BiVO_4$ photoanodes. As compared with the J^{OER} for the Mo:$BiVO_4$ w/o PEG photoanodes (1.2 mA cm^{-2}), both Mo:$BiVO_4$ PEG 200 and Mo:$BiVO_4$ PEG 300 photoanodes exhibited a dramatically enhanced J^{OER} of 2.2 and 1.7 mA cm^{-2} at 1.23 V_{RHE}, respectively, whereas Mo:$BiVO_4$ PEG 400 showed a lower J^{OER} (0.9 mA cm^{-2}). Moreover, the values obtained from LSV measurement for Mo:$BiVO_4$ photoanodes matched the calculated photocurrent achieved by integrating the IPCE over the light spectrum well (Fig. 4c). The IPCE for the Mo:$BiVO_4$ PEG 200 photoanodes exhibited the highest value of 46%, followed by Mo:$BiVO_4$ PEG 300 (36.5%), Mo:$BiVO_4$ w/o PEG (26%), and Mo:$BiVO_4$ PEG 400 (20%). The J^{OER} can be theoretically expressed as $J^{OER} = J_{max} \times \eta_{abs} \times \eta_{bulk} \times \eta_{inj}$. Based on the calculated η_{abs} values (**Table S3**, Supplementary Information), it can be assumed that the PEC performance of Mo:$BiVO_4$ PEG photoanodes with respect to Mo:$BiVO_4$ w/o PEG can be improved by ~ 1.2 times. However, despite the nearly identical η_{abs} among the three Mo:$BiVO_4$ PEG photoanodes, water oxidation performance significantly differs presumably due to the microstructure-dependent η_{bulk} and η_{inj} values (i.e., the varying grain sizes and pore structures).

3.3. Understanding charge transport properties of nanostructured Mo:$BiVO_4$ photoanodes.

To determine η_{bulk}, we conducted LSV for the sulfite oxidation reaction (SOR) over Mo:$BiVO_4$ PEG photoanodes in 0.5 M potassium phosphate buffer solution containing 0.5 M Na_2SO_3 (pH = 7.1) under standard front-side illumination (1-sun AM 1.5 G). For SOR, the surface charge recombination is negligible due to the facile electrochemical oxidation reaction at the electrode/electrolyte interface, and hence, η_{inj} can be assumed to be 100% [3]. Therefore, in the case of SOR, the water oxidation performance is represented as $J^{SOR} = J_{max} \times \eta_{abs} \times \eta_{bulk}$. Under this circumstance, η_{bulk} of each photoanode can be obtained by dividing the photocurrent density value obtained from SOR (J^{SOR}) by the maximum achievable photocurrent density (see Experimental Section for details). In case of Mo:$BiVO_4$ w/o PEG with compact film morphology, we obtained the η_{bulk} of 59 % at 1.23 V_{RHE} (**Fig. S5**, Supplementary Information). It has been reported that the compact and preferentially [0 0 1]-oriented $BiVO_4$ exhibited the η_{bulk} up to ~ 96 % at 1.23 V_{RHE}, but a sophisticate of fabrication technology was required compared to facile sol–gel process [16]. Hereafter, for further analyses, we mainly considered three types of Mo:$BiVO_4$ PEG photoanodes with similar thickness to demonstrate the variation of η_{bulk} depending on the grain size of sol–gel reaction based nanostructured $BiVO_4$ photoanodes.

The observed J^{SOR} showed a tendency similar to that of J^{OER} (Fig. 5a). At 1.23 V_{RHE}, the Mo:$BiVO_4$ PEG 200 photoanodes exhibited the highest J^{SOR} of 3.75 mA cm^{-2}, followed by 3.13 mA cm^{-2} (Mo:$BiVO_4$ PEG 300), and 2.07 mA cm^{-2} (Mo:$BiVO_4$ PEG 400). Moreover, as shown in Fig. 5b, it was found that the η_{bulk} of Mo:$BiVO_4$ PEG 200 was 72% at 1.23 V_{RHE}, followed by 62% (Mo:$BiVO_4$ PEG 300), and 42% (Mo:$BiVO_4$ PEG 400). A previous report indicated that the small pore size of a nanostructure did not impede the electrolyte penetration, so the hole injection from the photoelectrode to the electrolyte was not limited [37]. Therefore, it can be assumed that the difference in J^{SOR} observed for Mo:$BiVO_4$ PEG photoanodes results from different η_{bulk} among photoanodes, which originates not from the porosity-related surface area difference but from the grain size variation [41]. η_{bulk} represents the fraction of photogenerated holes that are transferred to the electrolyte interface without bulk recombination. Therefore, the decreased η_{bulk} indicates more charge recombination before participating in the oxidation reaction.

To gain an understanding of the η_{bulk} for Mo:$BiVO_4$ PEG photoanodes, electrochemical impedance spectroscopy (EIS) was performed under the same SOR electrolyte. To prevent dark electrolysis of sulfites, EIS was conducted at the applied potential of 0.8 V_{RHE} with 1-sun illumination in the frequency range of 100 kHz to 1 Hz [42]. Nyquist plots for all Mo:$BiVO_4$ PEG photoanodes exhibited one arc in the entire frequency range (Fig. 5c). To fit the EIS results, we employed an equivalent circuit model consisting of one R_s and serially connected R_p with parallel combination of constant phase element (CPE) (inset in Fig. 5c). Here, R_p

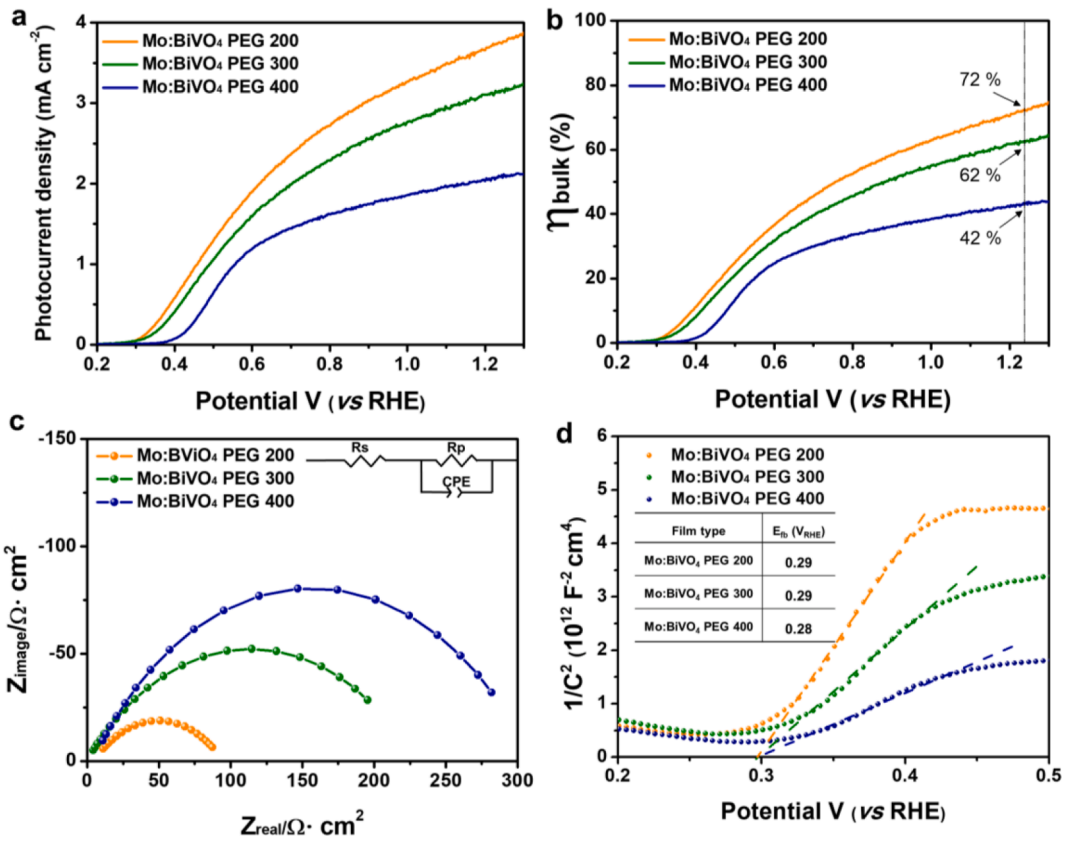

Fig. 5. a) J^{SOR} for Mo:$BiVO_4$ PEG 200 (orange), Mo:$BiVO_4$ PEG 300 (green), and Mo:$BiVO_4$ PEG 400 (navy) measured in 0.5 M KPi containing 0.5 M Na_2SO_3 (pH = 7.1) under front-side 1-sun illumination at scan rate of 20 mV s^{-1}. b) Bulk charge separation efficiency (η_{bulk}) of all Mo:$BiVO_4$ photoanodes; Mo:$BiVO_4$ PEG 200 (orange), Mo:$BiVO_4$ PEG 300 (green), and Mo:$BiVO_4$ PEG 400 (navy). c) EIS of Mo:$BiVO_4$ PEG 200 (orange), Mo:$BiVO_4$ PEG 300 (green), and Mo:$BiVO_4$ PEG 400 (navy). EIS measured under standard 1-sun solar illumination (AM 1.5 G) at 0.8 V_{RHE} containing 0.5 M Na_2SO_3 (pH = 7.1). The inset in Fig. 5c represents the equivalent circuit used for fitting the impedance results. d) M−S plot measured in 0.5 M KPi (pH = 7.0) under dark conditions with frequency of 1 kHz. (For interpretation of the references to colour in this figure legend, the reader is referred to the web version of this article.)

can be interpreted as the total resistance of charge transport and recombination in the bulk absorber layer due to negligible charge transfer resistance, as supported by the absence of the low-frequency arc (~1 Hz) in the Bode plot (**Fig. S6**, Supplementary Information) [43]. The fitting results are listed in **Table S4** (Supplementary Information). Mo:$BiVO_4$ PEG 400 showed the largest arc, and its size further decreased from the Mo:$BiVO_4$ PEG 300 to Mo:$BiVO_4$ PEG 200 photoanodes. A large arc in the Nyquist plot (i.e., high R_p value) indicates severe impediment of charge transport in Mo:$BiVO_4$ PEG 400 photoanodes having the smallest grain size. As the charge transport and charge separation behaviors in the photoelectrode are closely related to grain boundaries, the reduced J^{OER} and η_{bulk} for the Mo:$BiVO_4$ PEG 400 photoanodes are attributed to the small grain size–induced grain boundary scattering [37]. Moreover, the higher charge separation efficiency and better PEC performance associated with the Mo:$BiVO_4$ PEG 200 photoanodes than other Mo:$BiVO_4$ PEG photoanodes likely originate from the reduced grain boundary scattering owing to the larger grain size, so that more photogenerated holes are able to participate in the water oxidation reaction without bulk recombination.

Significant energy band bending can occur within large-sized photocatalysts, which in turn enhances the charge separation [17]. In this regard, the enhanced η_{bulk} of Mo:$BiVO_4$ PEG photoanodes with large grain size can be ascribed not only to the reduced grain boundary scattering but also to the large surface band bending. To investigate the surface band bending tendency for Mo:$BiVO_4$ PEG photoanodes, we firstly calculated the space charge region width (W_d). If the grain size radius (r_o) is larger than W_d , the surface band bending potential (V_{BB}) can be expressed as $V_{BB} = \frac{eN_dW_d^2}{2\varepsilon_o\varepsilon_r}$ where e is the electron charge, ε_o is the vacuum permittivity, and ε_r is the relative permittivity of $BiVO_4$ (~86) [44]. On the other hand, for the grain size in which the condition of $r_o < \sqrt{3}W_d$ is satisfied, the surface band bending potential is represented by $V_{BB} = \frac{er_o^2N_d}{6\varepsilon_o\varepsilon_r}$ [45]. From the classical solid state physics theory, W_d can be expressed as follows:

$$W_d = \sqrt{\frac{2\varepsilon_o\varepsilon_r(E - E_{fb})}{eN_d}} \quad (12)$$

where E represents the applied potential, E_{fb} represents the flat band potential, and N_d represents the donor density. To obtain N_d and E_{fb} of Mo:$BiVO_4$ PEG photoanodes, we conducted Mott-Schottky (M−S) analysis under dark conditions with a fixed frequency of 1 kHz under 0.5 M KPi (pH = 7). As shown in Fig. 5d, all the Mo:$BiVO_4$ PEG photoanodes showed a positive slope, indicative of n-type semiconductor characteristics. The E_{fb} , determined by the extrapolation of linear region, of Mo:$BiVO_4$ PEG photoanodes was around 0.3 V_{RHE}, which is consistent with the onset potentials for OER of those photoanodes. The N_d values of the Mo:$BiVO_4$ PEG photoanodes obtained from the M−S analysis were 3.75 × 10^{17} cm^{-3} for Mo:$BiVO_4$ PEG 200, 4.61 × 10^{17} cm^{-3} for Mo:$BiVO_4$ PEG 300, and 5.54 × 10^{17} cm^{-3} for Mo:$BiVO_4$ PEG 400. In addition, the calculated W_d at 1.23 V_{RHE} was 154 nm, 141 nm and 126 nm for Mo:$BiVO_4$ PEG 200, Mo:$BiVO_4$ PEG 300 and Mo:$BiVO_4$ PEG 400, respectively. Assuming r_o as a half of the average grain size obtained from image analysis (Table S1), it is confirmed that all Mo:$BiVO_4$ PEG photoanodes satisfy $r_o < \sqrt{3}W_d$, therefore V_{BB} could be obtained from the equation $V_{BB} = \frac{er_o^2N_d}{6\varepsilon_o\varepsilon_r}$. The V_{BB} value was determined

as 0.25 V for Mo:$BiVO_4$ PEG 200, 0.19 V for Mo:$BiVO_4$ PEG 300, and 0.11 V for Mo:$BiVO_4$ PEG 400, respectively. As large internal electric fields such as V_{BB} develop at the electrode and electrolyte interface, the more photogenerated carriers can be easily separated to participate in the OER without recombination. Clearly, the higher PEC performance of the Mo:$BiVO_4$ PEG 200 photoanodes is associated with its large grain size effect, enabling not only the reduced charge recombination due to less grain boundary scattering but also the enhanced η_{bulk} owing to the development of a large interfacial built-in potential [46].

3.4. H_2 treatment of the Mo:$BiVO_4$ PEG 200

To further improve the PEC performance of the Mo:$BiVO_4$ PEG 200 photoanodes, we performed hydrogen (H_2) treatment. A previous study demonstrated that the introduction of H_2 into $BiVO_4$ could enhance the PEC performance by increasing the overall electrical conductivity due to the created oxygen vacancies that act as shallow donors in n-type semiconductor materials [47]. To optimize the treatment temperature, the J^{SOR} values were determined by varying the H_2 treatment temperatures from 200 to 300 °C. At 250 °C, the highest J^{SOR} value of 4.7 mA cm^{-2} at 1.23 V_{RHE} and an onset potential of about 0.3 V_{RHE} were observed under standard 1-sun front illumination (**Fig. S7a**, Supplementary Information). There were no significant changes in morphology, crystal structure, or optical characteristics after H_2 treatment (**Fig. S7b–d**, Supplementary Information). Fig. 6a compares η_{bulk} for Mo:$BiVO_4$ PEG 200 before and after H_2 treatment (denoted as H, Mo:$BiVO_4$ PEG 200). η_{bulk} of H, Mo:$BiVO_4$ PEG 200 reached 89% at 1.23 V_{RHE}, ~12.3% higher than Mo:$BiVO_4$ PEG 200. The relative concentration of oxygen vacancy was characterized using XPS performed on both Mo:$BiVO_4$ PEG 200 and H, Mo:$BiVO_4$ PEG 200 (**Fig. S8**, Supplementary Information). The O 1 s peak of Mo:$BiVO_4$ can be fitted into three deconvoluted peaks at 530.0, 531.1 and 532.1 eV, corresponding to O^{2-} in the lattice (O_L), oxygen vacancy (O_V), and adsorbed/dissociated oxygen from water molecules (O_C) [48]. After H_2 treatment, we observed that all Bi 4f, V 2p, Mo 3d and O1s peaks shifted to lower binding energies, implying the increment of the electron density of each atom due to the formation of oxygen vacancies [49,50]. The relative O_V concentration, calculated based on the portion of O_V peak areas, was 9.98% and 12.05% for Mo:$BiVO_4$ PEG 200 and H, Mo:$BiVO_4$ PEG 200, respectively. Therefore, the η_{bulk} improvement could be attributed to the improved electrical conductivity of Mo:$BiVO_4$ PEG 200 because of high oxygen vacancy concentration after H_2 treatment.

3.5. Decoration of NiFeOOH catalyst on the H, Mo:$BiVO_4$ photoanode.

Despite of the η_{bulk} enhancement after H_2 treatment, the J^{OER} of H, Mo:$BiVO_4$ PEG 200 was still low (Fig. 6b), implying that the surface OER kinetics should be further improved for high PEC performance. To expedite the OER kinetics, NiFeOOH was deposited as an OER catalyst using the photo-assisted LSV method (see details in Experimental Section) [8]. The optimized H, Mo:$BiVO_4$ PEG 200/NiFeOOH exhibited remarkable enhancement in water oxidation performance including an onset potential of ~ 0.4 V_{RHE}, J^{OER} of 4.5 mA cm^{-2} at 1.23 V_{RHE} compared to the water oxidation performance of H, Mo:$BiVO_4$ PEG 200 photoanodes under 1-sun front-side illumination in 0.5 M KPi electrolyte containing 0.01 M vanadium oxide (V_2O_5) (pH = 7.4). The calculated ABPE was also increased to 1.64% at 0.69 V_{RHE} for H, Mo:$BiVO_4$ PEG 200/NiFeOOH as compared to 0.41% at 0.91 V_{RHE} (H, Mo:$BiVO_4$ PEG 200) (Fig. 6c).

For direct observation of the morphology of H, Mo:$BiVO_4$ PEG 200/NiFeOOH, we performed transmission electron microscopy (TEM) analysis (Fig. 7). The high-resolution TEM image shows that NiFeOOH exists as an amorphous states, while the lattice fringe of 0.252 nm was clearly observed which ascribed to the (0 2 0) plane of crystalline $BiVO_4$ (Fig. 7b) [51]. The high-angle annular dark field (HAADF) image and

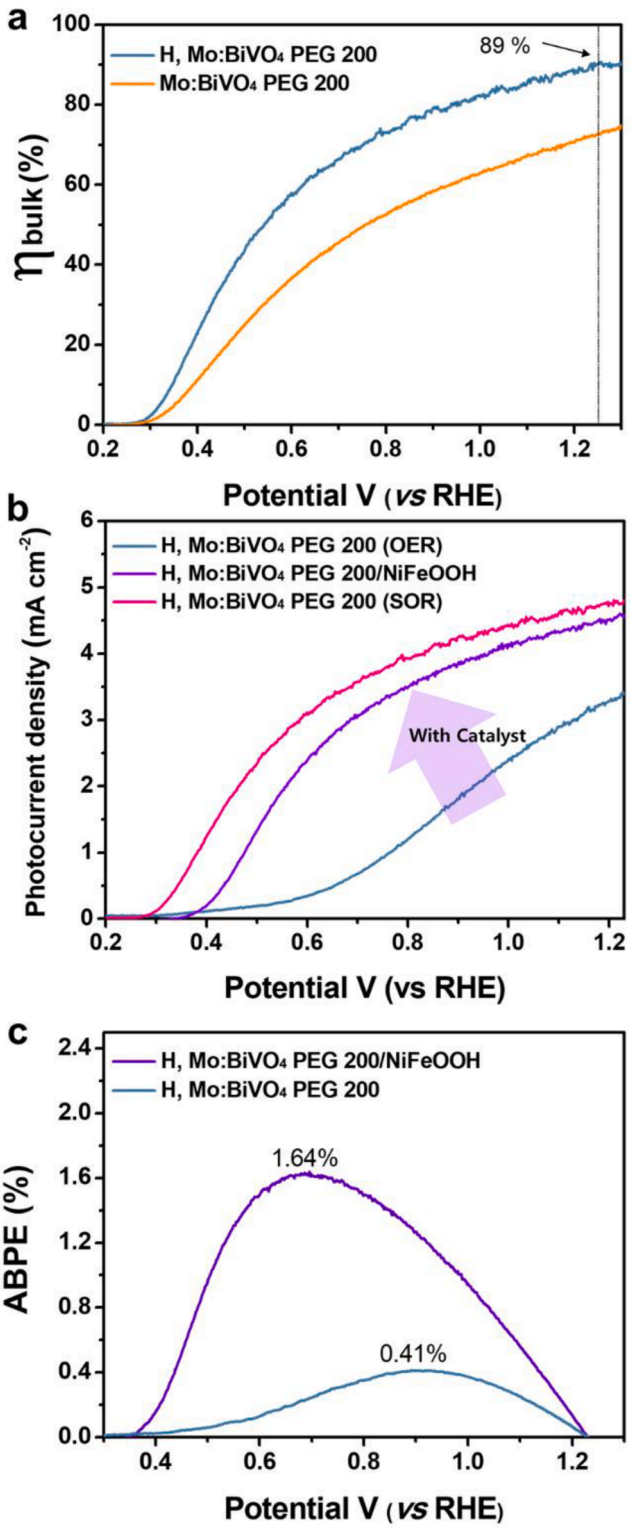

Fig. 6. a) Bulk charge separation efficiency (η_{bulk}) of H, Mo:$BiVO_4$ PEG 200 (light blue) and Mo:$BiVO_4$ PEG 200 photoanodes (orange). b) J^{SOR} of H, Mo:$BiVO_4$ PEG 200 measured in 0.5 M potassium phosphate in presence of 0.5 M Na_2SO_3 (pH = 7.1) (pink) and J^{OER} of H, Mo:$BiVO_4$ PEG 200 and NiFeOOH-decorated device (purple) measured in 0.5 M KPi containing 0.01 M V_2O_5 (pH = 7.4) electrolyte under standard 1-sun illumination at scan rate of 20 mV s^{-1}. c) Calculated maximum APBE of H, Mo:$BiVO_4$ PEG 200/NiFeOOH (purple) and H, Mo:$BiVO_4$ PEG 200 (light blue). (For interpretation of the references to colour in this figure legend, the reader is referred to the web version of this article.)

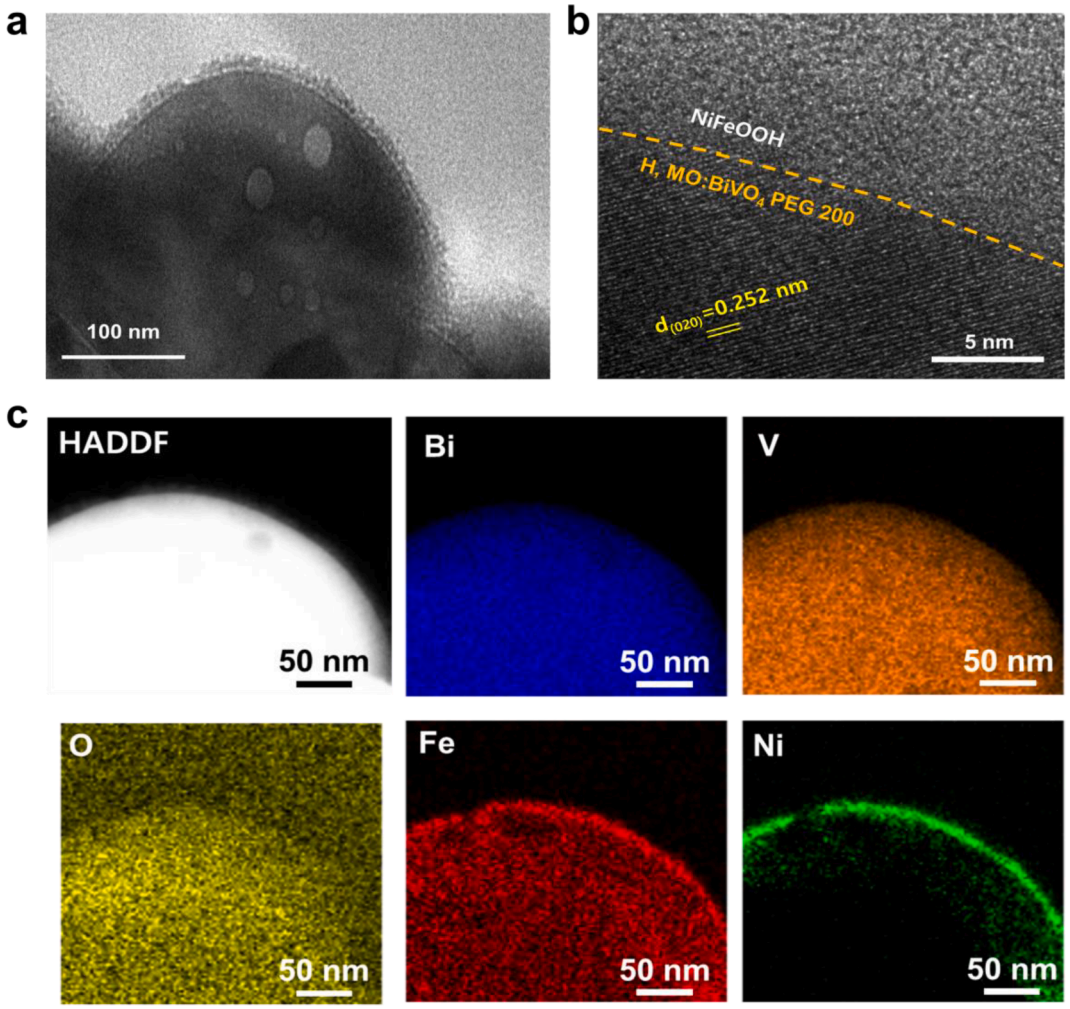

Fig. 7. a) Cross-sectional TEM images of the H, Mo:$BiVO_4$ PEG 200/NiFeOOH photoanode. b) HR-TEM image for the selected region. c) HADDF and STEM-EDS elemental mapping images for Bi, V, O, Fe, and Ni.

energy-dispersive X-ray spectroscopy (EDS) elemental mapping image clearly reveal the uniform distribution of Ni and Fe on the H, Mo:$BiVO_4$ PEG 200 photoanode (Fig. 7c).

The decoration of NiFeOOH catalyst was optimized by controlling the sweeping number and annealing. Among four candidates of Mo:$BiVO_4$ films that we fabricated (Fig. 2), it was confirmed that even after the identical processes of H_2 treatment and the NiFeOOH decoration, Mo:$BiVO_4$ PEG 200 exhibited the best PEC performance (**Fig. S9**, Supplementary Information). Moreover, the chemical states of NiFeOOH catalyst were confirmed by XPS. No peak shift was observed before and after annealing, while the Ni $2p_{3/2}$ (855.5 eV) and Ni $2p_{1/2}$ (873.2 eV) peaks and the Fe $2p_{3/2}$ (711.0 eV) and Fe $2p_{1/2}$ (724.5 eV) peaks with satellite signals were clearly observed which corresponds to Ni^{2+} and Fe^{3+}, respectively (**Fig. S10** a-c, Supplementary Information). The O 1 s peaks were observed at 529.6 eV, 531.1 eV and 531.8 eV which corresponds to O^{2-}, OH^-, and bounded water (H-O–H), respectively [52]. Moreover, the clear OH– peaks appeared in O 1 s spectra of H, Mo:$BiVO_4$ PEG 200 / NiFeOOH indicating that Ni and Fe exist as a form of NiFe (oxy)hydroxide (NiFeOOH) [53,54].

3.6. Stability of H, Mo:$BiVO_4$ PEG 200/ NiFeOOH photoanode

Finally, the photocurrent stability of H, Mo:$BiVO_4$ PEG 200/ NiFeOOH was evaluated in 0.5 M KPi + 0.01 M V_2O_5 (pH = 7.4) at 1.23 V_{RHE} under 1-sun front-side illumination. The H, Mo:$BiVO_4$ PEG 200/ NiFeOOH device showed excellent photocurrent stability, retaining ~ 90% of its initial photocurrent after 10 h irradiation, whereas H,Mo:$BiVO_4$ PEG 200 without catalyst exhibited not only low photocurrent density but also poor stability, showing almost full degradation within 5 h (Fig. 8a). Our PEC result was comparable to or higher than other previously reported $BiVO_4$-based photoanodes (**Table S5**, Supplementary Information). The oxygen (O_2) produced during the stability test was monitored by gas chromatography (GC) (Fig. 8b). The solid line represents the theoretical value assuming 100% Faradaic efficiency. The actual Faradaic efficiency was obtained by dividing the detected O_2 gas with the expected amount of O_2 calculated by the photocurrent density. The detected O_2 amount matched the theoretical value well, showing Faradaic efficiency of 82–96%. This result indicates that most photogenerated holes participated in the water oxidation reaction without detrimental recombination. The slightly lower Faradaic efficiency in the middle of measurement presumably resulted from the temporal adhesion of the generated O_2 on the surface of the photoelectrodes.

4. Conclusions

In summary, we introduced a facile nanostructuring strategy to fabricate nanoporous Mo:$BiVO_4$ photoanodes for enhancing charge separation efficiency and the water oxidation reaction. The grain and pore sizes of Mo:$BiVO_4$ film were controlled by using PEG with different molecular weights in the precursor solution. Large-molecular-weight PEG 400 within the wet film reduced the growth rate of nuclei by hindering ion addition, resulting in small-grain-sized Mo:$BiVO_4$ film during

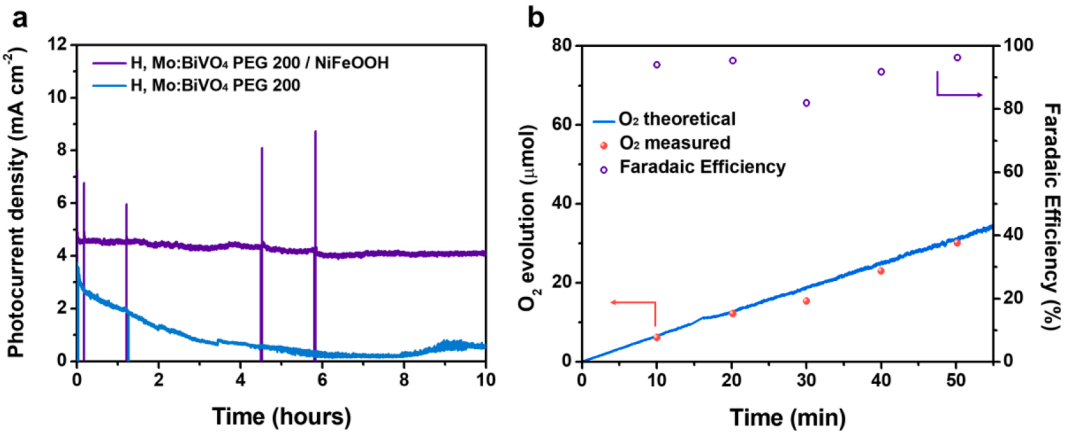

Fig. 8. a) Photocurrent stability test of H, Mo:$BiVO_4$ PEG 200 (light blue) and H, Mo:$BiVO_4$ PEG 200/NiFeOOH (purple) measured in 0.5 M potassium phosphate in presence of 0.01 M V_2O_5 (pH = 7.4) under AM 1.5 G illumination at 1.23 V_{RHE}. b) Produced O_2 as function of operation time during stability test for H, Mo:$BiVO_4$ PEG 200/NiFeOOH photoanodes. The solid blue line represents the theoretical value assuming 100% Faradaic efficiency, and the red circles indicate the experimentally detected oxygen production from GC analysis. The purple circles indicate actual Faradaic efficiency. (For interpretation of the references to colour in this figure legend, the reader is referred to the web version of this article.)

the crystallization process. By contrast, small-molecular-weight PEG 200 led to large-grain-sized nanoporous Mo:$BiVO_4$, exhibiting the enhanced η_{bulk} of ~ 72% and J^{OER} of ~ 2.2 mA cm^{-2} at 1.23 V_{RHE}. The improved PEC performance associated with large grain size can be understood in terms of the reduced charge recombination due to less grain boundary scattering as well as the large interfacial band bending potential. After the H_2 treatment, η_{bulk} increased up to 89% at 1.23 V_{RHE} due to passivation of the defect states, leading to the extended carrier lifetime. Finally, with deposition of NiFeOOH as an OER catalyst, the optimized H, Mo:$BiVO_4$ PEG 200/NiFeOOH exhibited remarkable enhancement in water oxidation performance including a J^{OER} of ~ 4.5 mA cm^{-2} at 1.23 V_{RHE} and an applied bias photon-to-current efficiency of 1.64% at 0.69 V_{RHE} with stable operation for 10 h. Our findings clearly suggest a facile low-cost approach to fabricate Mo:$BiVO_4$ photoanodes for highly efficient PEC water oxidation.

Declaration of Competing Interest

The authors declare that they have no known competing financial interests or personal relationships that could have appeared to influence the work reported in this paper.

Acknowledgements

This research was supported by the National R&D Program through the National Research Foundation of Korea (NRF) funded by the Ministry of Science and ICT (MSIT) (No. 2018M3D1A1058793, 2021R1A3B1068920, 2021M3H4A1A03049662, and 2021R1I1A1A01060058). This research was also supported by the Yonsei Signature Research Cluster Program of 2021 (2021-22-0002).

Appendix A. Supplementary data

Supplementary data to this article can be found online at https://doi.org/10.1016/j.cej.2021.133061.

References

[1] W. Yang, R.R. Prabhakar, J. Tan, S.D. Tilley, J. Moon, Chem. Soc. Rev. 48 (2019) 4979–5015.
[2] C. Ros, T. Andreu, J.R. Morante, J. Mater. Chem. A 8 (2020) 10625–10669.
[3] J.H. Kim, J.S. Lee, Adv. Mater. 31 (2019) 1806938.
[4] M. Ziwritsch, S. Muller, H. Hempel, T. Unold, F.F. Abdi, R. van de Krol, D. Friedrich, R. Eichberger, ACS Energy Lett. 1 (2016) 888–894.
[5] S.K. Cho, H.S. Park, H.C. Lee, K.M. Nam, A.J. Bard, J. Phys. Chem. C 117 (2013) 23048–23056.
[6] S.Y. Chae, C.S. Lee, H. Jung, O.S. Joo, B.K. Min, J.H. Kim, Y.J. Hwang, A.C.S. Appl, Mater. Interfaces 9 (2017) 19780–19790.
[7] S.J. Hong, S. Lee, J.S. Jang, J.S. Lee, Energy Environ. Sci. 4 (2011) 1781–1787.
[8] W. Yang, J.H. Kim, O.S. Hutter, L.J. Phillips, J. Tan, J. Park, H. Lee, J.D. Major, J. S. Lee, J. Moon, Nat. Commun. 11 (2020) 861.
[9] T.A. Kandiel, M.G. Ahmed, A.Y. Ahmed, J. Phys. Chem. Lett. 11 (2020) 5015–5020.
[10] R. Irani, P. Plate, C. Hohn, P. Bogdanoff, M. Wollgarten, K. Hoflich, R. van de Krol, F.F. Abdi, J. Mater. Chem. A 8 (2020) 5508–5516.
[11] Y. Park, K.J. McDonald, K.S. Choi, Chem. Soc. Rev. 42 (2013) 2321–2337.
[12] E. Samuel, B. Joshi, M.W. Kim, M.T. Swihart, S.S. Yoon, Nano Energy 72 (2020), 104648.
[13] S. Bera, S.A. Lee, W.J. Lee, J.H. Kim, C. Kim, H.G. Kim, H. Khan, S. Jana, H. W. Jang, S.H. Kwon, A.C.S. Appl, Mater. Interfaces 13 (2021) 14304–14314.
[14] M. Zhou, J. Bao, Y. Xu, J.J. Zhang, J.F. Xie, M.L. Guan, C.L. Wang, L.Y. Wen, Y. Lei, Y. Xie, ACS Nano 8 (2014) 7088–7098.
[15] H. Zhang, H.L. Li, Z.Y. Wang, Z.K. Zheng, P. Wang, Y.Y. Liu, X.Y. Zhang, X.Y. Qin, Y. Dai, B.B. Huang, Appl Catal. B 238 (2018) 586–591.
[16] H.S. Han, S. Shin, D.H. Kim, I.J. Park, J.S. Kim, P.S. Huang, J.K. Lee, I.S. Cho, X. L. Zheng, Energy Environ. Sci. 11 (2018) 1299–1306.
[17] H.L. Tan, R. Amal, Y.H. Ng, A.C.S. Appl, Mater. Interfaces 8 (2016) 28607–28614.
[18] Q. Qin, Q. Cai, C.Y. Jian, W. Liu, Sustain Energy Fuels 5 (2021) 1129–1133.
[19] Y.B. Kuang, Q.X. Jia, H. Nishiyama, T. Yamada, A. Kudo, K. Domen, Adv. Energy Mater. 6 (2016) 1501645.
[20] B.R. Lee, M.G. Lee, H. Park, T.H. Lee, S.A. Lee, S.S.M. Bhat, C. Kim, S. Lee, H. W. Jang, A.C.S. Appl, Mater. Interfaces 11 (2019) 20004–20012.
[21] J.H. Kim, Y.H. Jo, J.H. Kim, J.S. Lee, Nanoscale 8 (2016) 17623–17631.
[22] T.W. Kim, K.S. Choi, Science 343 (2014) 990–994.
[23] G. Jung, S. Byun, B. Shin, A.C.S. Appl, Energy Mater 3 (2020) 7756–7763.
[24] L.G. Xia, J.H. Li, J. Bai, L.S. Li, Q.Y. Zeng, Q.J. Xu, B.X. Zhou, Nanoscale 10 (2018) 2848–2855.
[25] H.C. He, S.P. Berglund, A.J.E. Rettie, W.D. Chemelewski, P. Xiao, Y.H. Zhang, C. B. Mullins, J. Mater. Chem. A 2 (2014) 9371–9379.
[26] C.C. Feng, Z.B. Jiao, S.P. Li, Y. Zhang, Y.P. Bi, Nanoscale 7 (2015) 20374–20379.
[27] J.K. Kim, K. Shin, S.M. Cho, T.W. Lee, J.H. Park, Energy Environ. Sci. 4 (2011) 1465–1470.
[28] D.P. Wang, C.W. Song, IEEE Access 8 (2020) 24941–24947.
[29] Z.Q. Li, Y.J. Xiong, Y. Xie, Inorg. Chem. 42 (2003) 8105–8109.
[30] L. Meda, G. Tozzola, A. Tacca, G. Marra, S. Caramori, V. Cristino, C.A. Bignozzi, Sol. Energy Mater. Sol. Cells 94 (2010) 788–796.
[31] K.R. Yoon, J.W. Ko, D.Y. Youn, C.B. Park, I.D. Kim, Green Chemistry 18 (2016) 944–950.
[32] D.B. Pedersen, M.Z. Zgierski, S. Anderson, D.M. Rayner, B. Simard, S.G. Li, D. S. Yang, J. Phys. Chem. A 105 (2001) 11462–11469.
[33] Y.C. Zhao, J. Wei, H. Li, Y. Yan, W.K. Zhou, D.P. Yu, Q. Zhao, Nat. Commun. 7 (2016) 10228.
[34] N.T.K. Thanh, N. Maclean, S. Mahiddine, Chem. Rev. 114 (2014) 7610–7630.
[35] A. Sharma, N. Liu, Q.S. Ma, H.Y. Zheng, N. Kawazoe, G.P. Chen, Y.N. Yang, Chem. Eng. J. 385 (2020), 123765.
[36] S. Singh, I.C. Maurya, P. Srivastava, L. Bahadur, J Solid State Electrochem 24 (2020) 2405.
[37] C.A. Bignozzi, S. Caramori, V. Cristino, R. Argazzi, L. Meda, A. Tacca, Chem. Soc. Rev. 42 (2013) 2228–2246.
[38] T.R. Bastami, M.H. Entezari, Q.H. Hu, S.B. Hartono, S.Z. Qiao, Chem. Eng. J. 210 (2012) 157–165.
[39] S. Tokunaga, H. Kato, A. Kudo, Chem. Mater. 13 (2001) 4624–4628.

[40] J.G. Cai, L.M. Qi, Mater Horiz 2 (2015) 37–53.
[41] H. Zhang, D. Li, W.J. Byun, X. Wang, T.J. Shin, H.Y. Jeong, H. Han, C. Li, J.S. Lee, Nat Commun 11 (2020) 4622.
[42] S. Xiao, H.N. Chen, Z.S. Yang, X. Long, Z.L. Wang, Z.L. Zhu, Y.Q. Qu, S.H. Yang, J. Phys. Chem. C 119 (2015) 23350–23357.
[43] H. Lee, W. Yang, J. Tan, Y. Oh, J. Park, J. Moon, ACS Energy Lett. 4 (2019) 995–1003.
[44] K.H. Ye, X. Yu, Z.G. Qiu, Y. Zhu, X.H. Lu, Y.M. Zhang, Rsc Adv 5 (2015) 34152–34156.
[45] Z. Zhang, J.T. Yates, Chem. Rev. 112 (2012) 5520–5551.
[46] Z.L. Tian, P.F. Zhang, P. Qin, D. Sun, S.N. Zhang, X.W. Guo, W. Zhao, D.Y. Zhao, F. Q. Huang, Adv. Energy Mater. 9 (2019) 1901287.
[47] J.H. Kim, Y. Jo, J.H. Kim, J.W. Jang, H.J. Kang, Y.H. Lee, D.S. Kim, Y. Jun, J.S. Lee, ACS Nano 9 (2015) (1829) 11820–11829.
[48] S.C. Wang, T.W. He, P. Chen, A.J. Du, K. Ostrikov, W. Huang, L.Z. Wang, Adv. Mater. 32 (2020) 2001385.
[49] J.B. Pan, B.H. Wang, J.B. Wang, H.Z. Ding, W. Zhou, X. Liu, J.R. Zhang, S. Shen, J. K. Guo, L. Chen, C.T. Au, L.L. Jiang, S.F. Yin, Angew. Chem. Int. Ed. Engl. 60 (2021) 1433–1440.
[50] T.W. Kim, Y. Ping, G.A. Galli, K.S. Choi, Nat. Commun. 6 (2015) 8769.
[51] J.J. Sun, X.Y. Li, Q.D. Zhao, M.O. Tade, S.M. Liu, J. Mater. Chem. A 3 (2015) 21655–21663.
[52] M.P. Suryawanshi, S.W. Shin, U.V. Ghorpade, J. Kim, H.W. Jeong, S.H. Kang, J. H. Kim, J. Mater. Chem. A 6 (2018) 20678–20685.
[53] M.P. Suryawanshi, U.V. Ghorpade, S.W. Shin, U.P. Suryawanshi, E. Jo, J.H. Kim, ACS Catal 9 (2019) 5025–5034.
[54] L. Cai, J. Zhao, H. Li, J. Park, I.S. Cho, H.S. Han, X. Zheng, ACS Energy Lett. 1 (2016) 624–632.